

Radiation Transport Simulations of Pulsational Pair-Instability Supernovae

KE-JUNG CHEN¹ AND WEIQUN ZHANG²

¹*Institute of Astronomy and Astrophysics, Academia Sinica, Taipei 10617, Taiwan*

²*Center for Computational Sciences and Engineering, Lawrence Berkeley National Lab, Berkeley, CA 94720, USA*

ABSTRACT

Massive stars of helium cores of $35 - 65 M_{\odot}$ eventually encounter the electron/positron creation instability, and it triggers explosive carbon or oxygen burning that produces several thermonuclear eruptions. The resulting catastrophe collisions of eruptive shells sometimes produce luminous transients with peak luminosity of $10^{43} - 10^{44}$ erg sec⁻¹, known as pulsational pair-instability supernovae (PPISNe). Previous 2D simulations of colliding shells show the development of Rayleigh-Taylor (RT) instabilities and mixing. Here we present radiation hydrodynamic PPISNe simulations of a $110 M_{\odot}$ solar-metallicity star that was promising to produce a superluminous transit in the early work. Our comprehensive study contains a suite of one-, two-, and three-dimensional models. We discuss the impact of dimensionality and fluid instabilities on the resulting light curves. The results show the RT mixing found in previous multidimensional hydro studies transforms into a thin and distorted shell due to radiative cooling. Radiation from the wiggly shell peaks at its bolometric light curve of $\sim 2 \times 10^{43}$ erg sec⁻¹, lasting about 150 days and following with a plateau of $\sim 3 \times 10^{42}$ erg sec⁻¹ for another two hundred days before it fades away. The total radiation energy emitted from colliding shells is $\sim 1.8 \times 10^{50}$ erg, which is $\sim 27\%$ of the kinetic energy of the major eruption. The dimensional effects also manifest on the physical properties, such as irregularity and thickness of the shell. Our study suggests PPISNe is a promising candidate of luminous SNe, the radiation of which originates from colliding shells with a homogeneous mixing of ejecta.

Keywords: Supernovae: general – Radiative transfer – Hydrodynamics – Fluid Instabilities

1. INTRODUCTION

The final helium core mass usually determines the fate of very massive stars (zero age main sequence mass $\geq 80 M_{\odot}$). When the mass of a forged helium core exceeds $\geq 35 M_{\odot}$, some pressure-supporting photons start to convert into electron-positron pairs during the central carbon/oxygen burning, which softens the equations of state by

reducing the adiabatic index, $\gamma < 4/3$. It then results in a contraction of the core, and the non-hydrostatic burning drives temperatures to pulsate at the dynamic time scale of a few hundred seconds. At this time, the pulsating in temperature produces only sonic waves without any destructive explosions. For stars having more massive helium cores of $45 - 65 M_{\odot}$, several strong eruptions triggered by pair-instabilities occur before the star finally collapses into a black hole. The later eruptions usually gain more energy from the explosive burning but carry less ejecta, which makes them

collide with the earlier ejecta and results in many interesting outcomes. They are called “pulsational pair-instability supernovae (PPISNe),” first introduced by Barkat et al. (1967), and are subjects of detailed studies done by Woosley et al. (2007); Woosley (2017).

As the helium core mass increases, the pulse becomes more energetic and ejects less mass, and the duration between pulses increases from a few hundred seconds to several years. Such an eruption starts to generate an SN-like transit at a helium core mass of about $45 M_{\odot}$. If the massive star still has a substantial hydrogen envelope before the eruption occurs, the first strong pulse carries energy of $10^{49} - 10^{50}$ erg and can easily blow out the hydrogen envelope with a binding energy of $10^{43} - 10^{44}$ erg and produce a faint Type IIP SN. However, subsequent pulses colliding with the first one can produce a much brighter Type IIn SN. If no hydrogen envelope remains at the time of eruptions, the collision of helium mass shells may produce a luminous Type I SN. For the helium core mass ranging from 45 to $55 M_{\odot}$, the duration between pulsations becomes about several years, and the shell collisions would happen at $10^{15} - 10^{16}$ cm from the center of the star, assuming ejecta are moving at a speed of $\sim 1000 \text{ km sec}^{-1}$. In this circumstance, much of the collision energy dissipates in the optical emission. An energetic collision of 10^{51} erg pulse may result in a superluminous supernova (Inserra et al. 2016; Takahashi 2018, SLSNe) such as SN 2007bi (Gal-Yam et al. 2009). Recent stellar evolution models by Woosley (2017); Leung et al. (2019) confirmed a broad variety of outcomes of PPISNe. Their consequent radiation properties studied by Woosley et al. (2007); Dessart et al. (2015); Moriya & Langer (2015); Smidt et al. (2015); Jerkstrand et al. (2016); Woosley (2017) showed that PPISN can provide outcomes ranging from several faint transit events to 1-2 SLSNe.

The newly discovered SN IPTF14hls (Arcavi et al. 2017), which has a long-duration and multi-peak light curve, poses a grand challenge to our

understanding of its emission mechanics. It is likely associated with multi-collisions of circumstellar interactions that can be explained naturally by PPISNe (Woosley 2018). Another possibility for such dramatic changes in the light curves (LCs) may be due to the asymmetry of ejecta that leads to the formation of clumpy structures and results in the inhomogeneous emissions.

Woosley et al. (2007) modeled a PPISN of a $110 M_{\odot}$ star of solar metallicity with the 1D KEPLER code (Weaver et al. 1978; Heger et al. 2001) to explain the light curve of SN 2007bi. A detailed follow-up study (Woosley 2017) showed the diversified and enriched outcomes of PPISNe. However, in these 1D simulations, a large-density spike always formed during the shell collisions due to rising fluid instabilities. However, a fundamental deficiency of 1D simulations is that they cannot address fluid instabilities from first principles. Chen et al. (2014) have performed the two-dimensional simulation of PPISN and showed that the development of Rayleigh-Taylor (RT) instabilities drives mixing between the colliding shells. The intrinsic nature of this problem requires radiation hydrodynamic (rad-hydro) simulations in at least two-dimensions (2D) with a sufficient spacial resolution to model the thin radiating region from the shell collision before the observational signatures of PPISNe can be properly calculated.

The results from previous hydrodynamic simulations may change significantly in the context of rad-hydro, in which radiation co-evolves the gas dynamics through radiative heating and cooling. Highly-resolved radiation transport simulations of colliding shells pushes the envelope of the state-of-the-art astrophysical simulations. They require robust numerical algorithms and substantial supercomputing resources of millions of CPU hours to achieve.

Since we are not sure of the detailed emission spectra from PPISNe, the radiation is presumably coming from the thermal radiation during the shell collisions. As the first step, we use a single group

of radiation transport (gray-approximation) based on the frequency-integrated formulation of the rad-hydroequations. It provides a good starting point for studying the radiation emission and its impact on the dynamics of ejecta. To examine the PPISN radiation properties in great detail, we performed one-, two-, and three- dimensional radiation transportation simulations and compared them with the previous hydro simulations. Thus, the comparison provides a deeper understanding of the PPISN and its observational signatures.

We describe our numerical approaches to the rad-hydro simulations in Section 2 and then present the results of 1D, 2D, and 3D models in Sections 3, 4, and 5, respectively. The significance and applications of our results are discussed in Section 6, and the conclusions are given in Section 7.

2. PPISN MODEL / NUMERICAL METHOD

We take a fiducial case the PPISN studied in Woosley et al. (2007); Chen et al. (2014), whose progenitor was a solar-metallicity star with the zero-age main sequence mass of $110 M_{\odot}$. When this star evolved to the post-main sequence with a helium core mass of $49.9 M_{\odot}$, the first energetic pair-instability eruption occurred and ejected most of its hydrogen envelope, making a faint Type II supernova and leaving a residual of $50.7 M_{\odot}$. The helium core again encountered the pair instability, twice in rapid succession, at 6.8 years after the first eruption. The second and third eruptions ejected $5.1 M_{\odot}$ gas with a kinetic energy of 6×10^{50} erg. This star produced three major pair-instability (PI) pulses, P1, P2, and P3. P3 collided with P2, and the merged ejecta started to catch up to P1 at $r \sim 10^{15}$ cm at a speed of a few 1000 km sec^{-1} . During the catastrophic collisions that occurred at this time, part of the kinetic energy of the ejecta transformed into radiation.

To study the collisions among the three eruptions, we mapped this progenitor star calculated by 1D stellar evolution KEPLER (Weaver et al. 1978; Heger & Woosley 2002) onto the rad-hydro code, CASTRO, when all three eruptions are present. At

this time, the forward shock of P1 has propagated to $r \sim 2 \times 10^{16}$ cm. Woosley et al. (2007) suggested that most of the radiation from the collision between P2/P3 and P1 is emitted when the shock of P2+P3 has reached $r \sim 1. \times 10^{16}$ cm; that marks the finish point of our simulations.

2.1. CASTRO

CASTRO is a multidimensional adaptive mesh refinement (AMR) code designed exclusively for astrophysical simulations (Almgren et al. 2010; Zhang et al. 2011). It uses an unsplit piecewise parabolic method (PPM) hydro scheme (Colella & Woodward 1984) with multi-species advection. We use γ law equation of state (EOS) ($\gamma = 5/3$ for the ideal gas), which is sufficient for the colliding shell problems. The ideal gas EOS is a good approximation for the colliding PPISNe gas, which is not as extreme as that in the core of stellar explosions, which requires the degenerate electrons and Columb corrections, such as the Helmos EOS Timmes & Swesty (2000).

Densities, velocities, temperatures, and mass fractions of elements from the 1D KEPLER model are mapped in the CASTRO AMR grids with a conservative scheme developed by Chen et al. (2011); Chen et al. (2013), which conserves physical quantities such as energy and mass during the mapping. Self-gravity uses a monopole approximation by constructing a 1D gravitational potential from the radial average of the density, then calculates gravitational force for each AMR grid. Such an approximation remains valid, while the global spherical symmetry of ejecta does not break down much. To track the mixing of elements, we follow the evolution of four different species of ^1H , ^4He , ^{12}C , and ^{16}O , which are domain elements in the ejecta. Please note that the eruptions of PPISNe are mainly driven by the central ^{16}O burning; therefore, elements of ^{28}Si , ... to ^{56}Ni are invisible. The detailed setup for 1D, 2D, and 3D rad-hydro simulations is described in the following section.

2.2. Radiation Hydrodynamics

The rad-hydro solver in CASTRO uses the mixed-frame approach and adopts the flux-limited diffusion (FLD) and local thermodynamic equilibrium assumptions. The detailed formulation can be found in (Zhang et al. 2011, 2013). It uses a second-order explicit Godunov method for the hyperbolic part of the system and a first-order backward Euler method for the parabolic part. The rad-hydro version of CASTRO has been used to address a wide range of rad-hydro problems in the astrophysics context, such as neutrino-driven explosions in the core-collapse SNe (Dolence et al. 2015) and SNe shock breakout problems (Lovegrove et al. 2017). The major advantage of CASTRO is its efficiency due to the use of AMR combined with a good scaling behavior on modern supercomputers up to 30,000 CPU cores, which are more efficient than other rad-hydro codes, for example, ZEUS-MP (Hayes et al. 2006), Orion (Krumholz et al. 2007), HERACLES (González et al. 2007), V2D (Swesty & Myra 2009), RAMSES (Commerçon et al. 2011), and CRASH (van der Holst et al. 2011). A unique strength of CASTRO is that its hyperbolic solver uses an unsplit version of the PPM method that avoids spurious noise caused by dimensional splitting. CASTRO is based on a mixed-frame formulation, similar to that of Orion. A main advantage of the mixed-frame approach is its strict energy conservation, whereas its drawback is in limited use for line transport. However, line transport cannot be treated by a gray radiation solver regardless of the choice of frame. Compared with the two-moment approach, the FLD approach is computationally cheaper, and it uses much less memory for the multi-group radiation. However, it carries low accuracy for optically-thin flows. For the current setup, we use a gray approximation based on the frequency-integrated formulation of the rad-hydro equations. A multi-group rad-hydro is much more computationally expensive and needs to be supported by realistic opacities. Therefore, we defer it for a future study.

2.3. Opacities

Opacities determine how the radiation interacts with gas by emission, absorption, or scattering; that is important to any rad-hydro simulations. Realistic opacities can be calculated based on the gas temperature, density, composition of elements, and ionization states. As a starting point, we employ simple scattering and absorption opacities by assuming

$$\kappa = \kappa_0 \rho^m T^{-n} \nu^p, \quad (1)$$

where κ is either Planck or Rosseland mean opacities, κ_0 is a constant, ρ is gas density, T is gas temperature, ν is radiation frequency, and m , n , and p are constants. κ has the unit of cm^{-1} . For the gray solver, the opacities are made independent of radiation frequency by setting p to zero. CASTRO allows for two temperatures (different radiation and gas temperature, so $E_r \neq aT_{\text{gas}}^4$). Correspondingly, CASTRO takes both the Planck mean, κ_P , and Rosseland mean, κ_R , opacities—these have different weightings. If we set $\kappa_P \Delta x \gg 1$ (κ_P is large), Δx is the zone size in the simulation, and then the two temperatures become the same. Scattering contributes Rosseland mean but not Planck mean. In our CASTRO run, we set κ_R to Thomas scattering at a sufficiently high temperature, which can be expressed as

$$\kappa_T = 0.2(1+X) \text{ cm}^2 \text{ g}^{-1}, \quad (2)$$

where X is the hydrogen mass fraction. Units of opacities in CASTRO are cm^{-1} , $\kappa_R = \kappa_T \rho$ where ρ is gas density, so we parameterize $\kappa_T = 0.1, 0.2, 0.3$, and 0.4 by assuming different hydrogen mass fractions or the ionized environment. Ideally, we would like to use realistic opacities based on a table or solve the ionization states of the multi-species gas; however, doing so creates a great challenge in the simulations of colliding shells. In PPISNe, radiation originates from colliding shells and likely propagates inside the clumpy ejecta. Therefore, the gas density can be highly inhomogeneous and anisotropic, so it causes the opaci-

ties to vary significantly along the line of sight for the outgoing photons. Because the opacities in FLD scheme are derived in the diffusion approximation to the radiation transport equation, the code prefers the isotropic and homogeneous gas field in the length scale comparable to the photon mean free path. Sudden changes in opacities easily makes the rad-hydro simulations numerically unstable, which leads to the crash of the simulations. Therefore, on the first attempt, we use the simple opacities of Thomas scattering. Even so, the advancing rad-hydro time step remains tiny. Evolving our 2D/3D rad-hydro simulations for a time scale of $\sim 300 - 400$ days requires $10^5 - 10^6$ time steps to complete each run, which makes these simulations very computationally expensive. We have spent about three million CPU hours running these models (mainly for the 2D and 3D simulations) on two powerful Cray XC-40 supercomputers: Edison ($\sim 134,000$ CPU cores) at the National Energy Research Scientific Computing Center (NERSC) and Aterui ($\sim 25,000$ CPU cores) at the National Astronomical Observatory of Japan (NAOJ). The single 3D run consumed more than 1.5 million CPU hours.

2.3.1. 1D Setup

1D CASTRO uses a spherical symmetry coordinate, r , with a reflect and outflow at the inner and outer boundaries, respectively. In 1D runs, we use different resolutions of 1024, 4096, and 8192 uniform grids with a domain size of $r = 2 \times 10^{16}$ cm to examine the 1D results under different resolutions and opacities.

2.3.2. 2D Setup

2D CASTRO uses a cylindrical grid, r and z . We simulate only one quadrant of the star; therefore, the outflow and reflecting boundary conditions are set on the upper and lower boundaries in r and z , respectively. The root grid has 512^2 zones with three levels of refinement for an additional factor of up to 8 (2^3) in the spatial resolution. The grids are refined based on gradients of density and ve-

locity. This setup provides an effective simulation domain of $4,096 \times 4,096$ zones to cover a domain of $[2 \times 10^{16}]^2$ cm².

2.3.3. 3D Setup

3D CASTRO uses a cartesian grid, x , y , and z . We simulate a full star with 4π geometry in 3D. Thus, the outflow boundary conditions are on all boundaries. The root grid has 512^3 zones and up to two levels of refinement for an additional factor of two in spatial resolution. The refinement criteria are the same as 2D cases. This setup provides $2,048 \times 2,048 \times 2,048$ zones for the simulation domain of $[2 \times 10^{16}]^3$ cm³ while the star is located at the center of the simulated box.

2.4. Light Curve Calculation

We calculate the LCs by collecting the radiation flux at the boundary of our simulation domain and assume the photons start free-streaming from it. The LCs can be expressed as

$$L = 4\pi r_p^2 F_{rad}, \quad (3)$$

where L is the luminosity in erg s⁻¹, F_{rad} is the radiation flux in erg cm⁻² sec⁻¹ at the photosphere, and r_p is cm located at the boundary of the simulated box. The barometric LCs can be calculated directly from our simulations.

3. 1D RESULTS

3.1. 1D PPISN Evolution

1D simulations provide a direct physical picture of the dynamics of ejecta and serve as a good starting point for our rad-hydro runs. At the beginning of 1D simulations, peak velocities of P2 and P3 are $\sim 3.9 \times 10^7$ cm sec⁻¹ at $r \approx 7.9 \times 10^{14}$ cm and $\sim 4.8 \times 10^7$ cm sec⁻¹ at $r \approx 3.2 \times 10^{14}$ cm, respectively. In the previous pure hydro simulation of [Chen et al. \(2014\)](#), the faster-moving P3 overtakes P2 within 50 days and has completely merged with it at $r \approx 2.3 \times 10^{15}$ cm, then together they collide into P1. In the rad-hydro simulations, the photons diffusing from P2 and P3 generate radiative cooling and lead to the production of two thin shells

(density spikes in 1D) before their merger. This radiative cooling also decelerates the shock velocities of P2 and P3. Radiation starts diffusing out and turning into the LCs. The merger of the two pulses takes place at $r \approx 5.1 \times 10^{15}$ cm at 130 days. There is a sudden jump in the radiation flux ahead of the shock front of P2 through free-streaming photons before it merges with P3 or P2+P3. We show the evolution of velocity, gas density, radiation energy, and radiation flux of 1D PPISNe in Fig. 1. Density spikes appear shortly after the simulation starts, and their density constraint is relative to its surrounding, $\Delta_S = \langle \frac{\delta \rho}{\rho} \rangle \sim 1,000 - 2,000$. Most of the radiation flux comes from the same location as the density spike, which indicates that the colliding of the shells produces a great deal of thermal radiation, and the ejecta ahead of the shell is heated up to a few 10^5 K. Depending on the energetics, masses, and duration between eruptions, the electromagnetic spectrum of colliding shells may range from radio to UV.

1D Lagrange rad-hydro codes, such as KEPLER (Weaver et al. 1978; Heger & Woosley 2002) or STELLA (Blinnikov et al. 2006), usually fail to resolve the structure of the density spike because of their spatial resolution, which is a few hundred to a thousand grids per model. A Eulerian code with many grids is required in order to achieve a high enough spatial resolution to probe the structure of the density spike. We use resolutions of 1024, 2048, and 8192 zones in the 1D runs and are able to reveal the detailed structure of the density spike. Fig. 2 shows the close-up of the spike in the instant that two pulses merge. The width of the density spike is about 1.4×10^{14} cm, and densities range from $\sim 8 \times 10^{-16} \text{ g cm}^{-3}$ to $\sim 1.1 \times 10^{-12} \text{ g cm}^{-3}$. The Δ_S is $\sim 1,375$, making it look like a spike in the entire simulation domain. This spike locates at the shock front, which creates a discontinuity in density, velocity, and radiation flux. Radiation directly streams out of the spike. The formation for a density spike in 1D usually implies the development of fluid instabilities because of the pil-

ing up of the gas. Due to the dimensional limitation, 1D models cannot follow the fluid instabilities from the first principles. We discuss how this spike transforms in the multidimensional rad-hydro simulations in later sections.

3.2. 1D Light Curves

A crucial goal of rad-hydro simulations is calculating the observational signatures. With the single group rad-hydro, we can obtain the bolometric LCs (total amount of radiation energy emitted in one band). However, the color information of LCs and the full spectra are unavailable. We show the effect of resolution to LCs in Fig. 3. The 1D LCs are from simulations of 1024, 4096, and 8192 zones with the same parameters. The LC results suggest that radiation flux is sensitive to its resolution. The lower-resolution runs (1024 zones) tend to yield a higher peak luminosity with a shorter light curve duration. The second peak in light curve appears in the higher-resolution runs — 4096- and 8192-zone runs—and the rising time of the second peak is earlier in the 4096-zone run. The 1D results of different resolutions suggest that its light curve about peak luminosity and duration of this $110 M_\odot$ PPISN is about $9 - 19.5 \times 10^{42} \text{ erg sec}^{-1}$ with a duration of 100–200 days. The rising time of the second peak should result from the collision of the two density spikes of P2 and P3; however, it is not resolved in the 1024-zone run. The resolution may affect the LCs through the numerical diffusion of photons that affect the flux from the photosphere.

Since our opacity setting is not realistic, we employ several constant opacities, $\kappa = 0.1, 0.2$, and 0.4 , to examine how the opacities change the 1D LCs in Fig. 4. In three cases, we use the highest resolution of the 8192-zone. With increased opacities, the peak of the LCs becomes broader with a shorter height. The second peak feature again appears in the high-resolved runs regardless of opacities. LCs peaks at $7 - 11.5 \times 10^{42} \text{ erg sec}^{-1}$ with a duration of 150–200 days. The separation between the first and second peak is about 150 days. The increasing opacities result in a longer diffu-

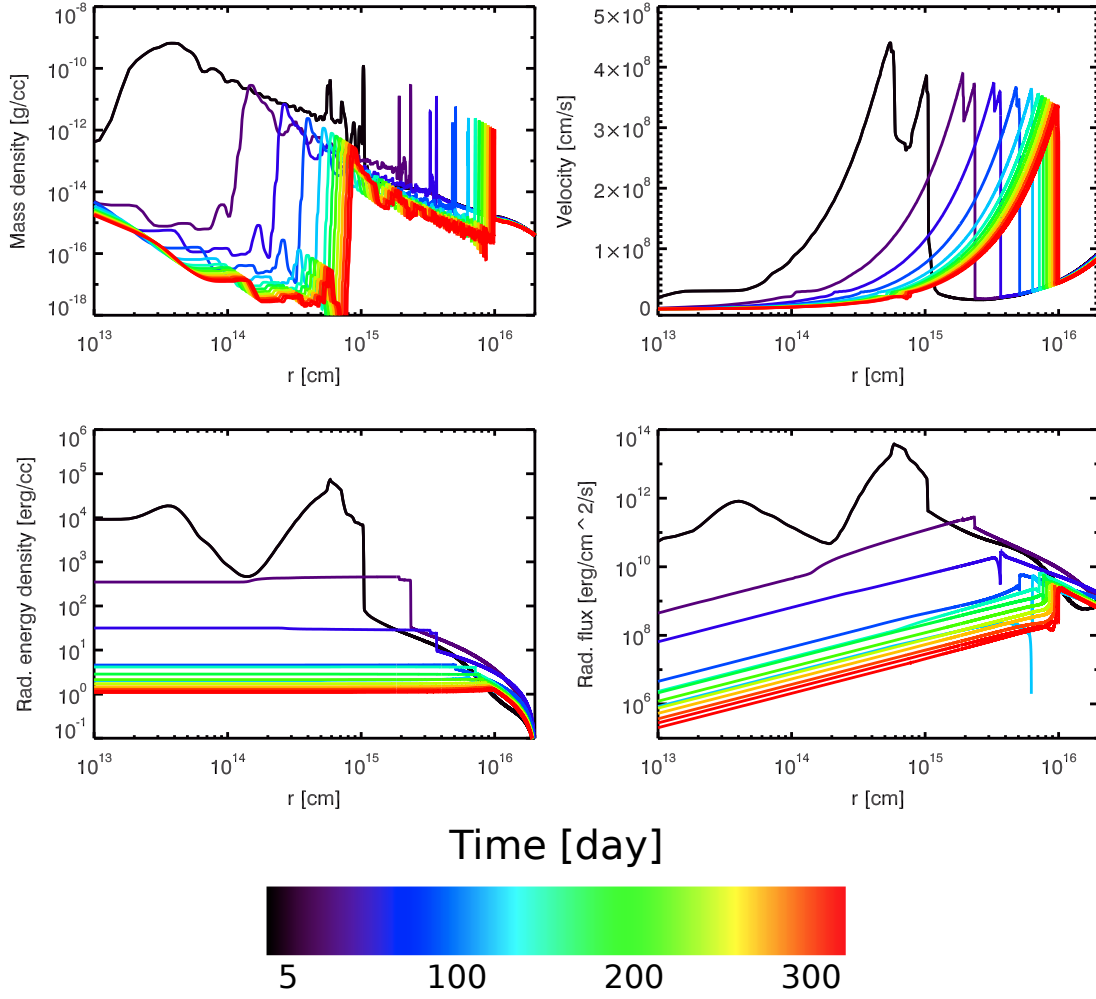


Figure 1. Evolution of a 1D PPISNe. Curves of different colors show the profiles of gas density, velocity, radiation, radiation energy density, and radiation flux from 5 - 333 days after the shell collisions. The high-resolution model of the 8192 zone is employed in this example. The collisions between two major shells can be seen in the velocity. Two large density spikes of P2 and P3 first appear, then merge into one. The peaks of radiation energy density and flux are also located around the density spikes.

sion time of photons and reflect in its observational signatures by broadening its LCs and lowering its peak luminosity. Opacities determine the decoupling of photons and gas; therefore, they affect LCs by deciding the location of the photosphere and its emitted radiation flux. In the realistic situations, LCs should be more sensitive to opacities. The 1D results suggest that our PPISN from a $110 M_{\odot}$ star have a characteristic peak luminosity of $7-19.5 \times 10^{42} \text{ erg sec}^{-1}$ with duration of 150–200 days and a second peak feature of $5-6 \times 10^{42} \text{ erg sec}^{-1}$ with a duration of about 50 days.

4. 2D RESULTS

4.1. 2D PPISN Evolution

1D results suggest the formation of a density spike in the colliding shells that is consistent with previous 1D rad-hydro results (Woosley et al. 2007; Woosley 2017). In this section, we investigate how the 1D spikes evolve in the 2D simulations. We first show the 2D evolution of $\kappa = 0.2$ in Fig. 5. At the beginning of the simulation, the original density structure is perfectly spherical-symmetrical. As time goes on, two distinct shells form from P2 and P3 (Fig. 5 (b)). The thin shells

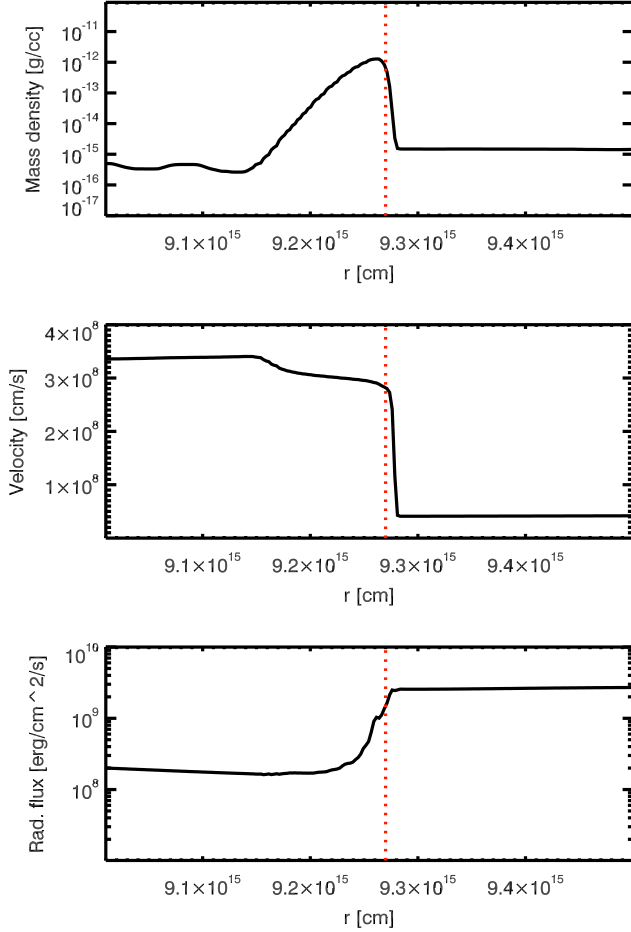


Figure 2. Zoom-in of the density spike at $t = 300$ days. The red-dashed line indicates the peak of the density spike. The width of the density spike is about 1.4×10^{14} cm, and it is resolved by 50 zones; the zone number for this model is 8192. The spike is sitting at the shock. Most of the radiation flux originates from this density spike.

form in the shock front due to radiative cooling. The shells are pushed by the hot ejecta. The velocity of the P2 shell is $\sim 2 \times 10^8$ cm sec $^{-1}$. We compare the early phase of the P2 and P3 collision for both rad-hydro and pure-hydro in Fig. 6. In the pure-hydro simulations (Chen et al. 2014), the merging shock from P2 and P3 collides with the P1 ejecta within 50 days. Due to the snowplowing mass ahead of the shock, a reverse shock forms to drive RT instabilities to mix up the ejecta behind it. However, for the rad-hydro model, the

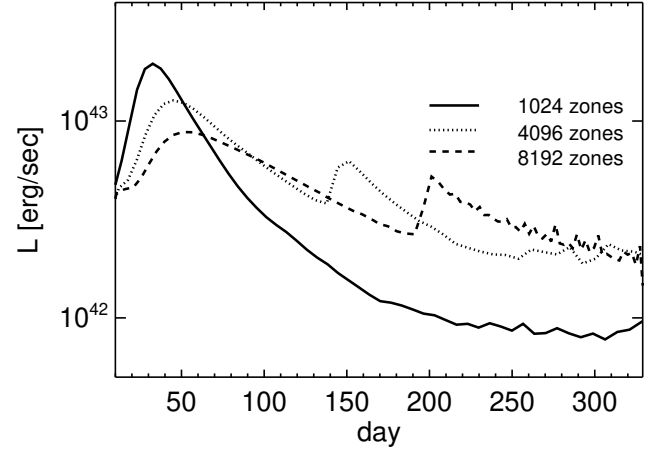


Figure 3. 1D LCs of different resolutions. As the spatial resolution increases, the peak luminosity decreases and its peak becomes broad. The second peak features appear only in higher-resolution runs. These 1D runs use $\kappa = 0.2$.

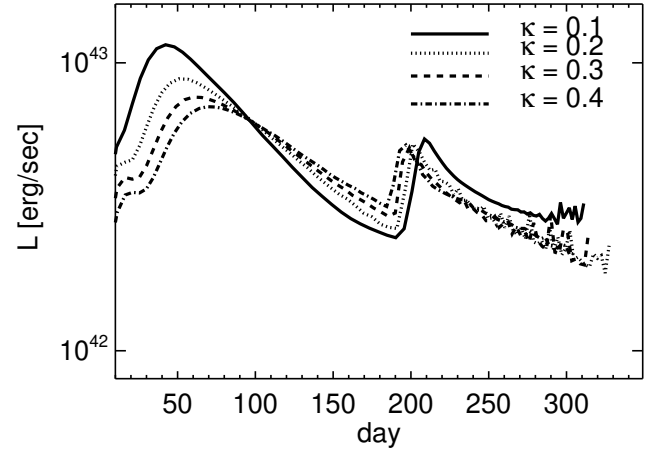


Figure 4. 1D LCs of different opacities in 8192-zone runs. Two peak signatures appear in these 1D LCs. The peak luminosity is $\sim 10^{43}$ erg sec $^{-1}$ and decreases as κ increases. LCs broaden as the peak luminosity drops, and the location of the peak shifts to a later time.

energy of the radiative shock quickly dissipates as it propagates. Thermal radiation from the collision between P2 and P3, together with that from P2 and P1, turns into photons to power the light curve of PPISNe. The outer shell where the radiation originates lacks spherical symmetry and deforms

as it moves out. See Fig. 6 for the comparison of 2D rad-hydro and pure-hydro models at 256 days. The shock features in the rad-hydro simulations seem to disappear. In the rad-hydro simulations, the shock propagating in nearly optically thin regions quickly dissipates its energy because the radiation diffuses from the shock front. The RT fingers of colliding shells found in the previous pure-hydro simulations are not prominent in the rad-hydro model due to the absence of a reverse shock to drive RT instabilities. However, the non-uniform heating and radiative cooling distort the spherical symmetry of the shell.

We compare 2D simulations of different opacities in Fig. 7. The density shell shows different width and inhomogeneity in different opacities, which suggests that the dynamic of the shell depends on the opacities. The radiation bursts out from the shell surface, which is deformed by radiative cooling. If the photosphere gets close to the emitting surface, the radiation becomes inhomogeneous and anisotropic, as shown in Fig. 8, and makes PPISNe LC sensitive to viewing angles.

4.2. 2D Light Curves

We show the 2D LCs in Fig. 9. The 2D LCs differ from 1D LCs in several places. The peaks of LCs from simulations of $\kappa = 0.1, 0.2$, and 0.4 all exceed 10^{43} erg sec $^{-1}$. They are slightly more luminous than their 1D counterparts, and the second peak seems to smooth out in 2D. Once the merging shell approaches the boundary of the simulated box (the assumed location of the photosphere), we start to see the variation of LCs that is reflected in the wiggly structure of the shell, which affects the radiation flux and the resulting LCs. If we use realistic opacities, the angle-dependent effects may appear at earlier times.

5. 3D RESULTS

5.1. 3D PPISN Evolution

The 1D and 2D results provide a quantitative understanding of the PPISNe. We would like to compare the realistic 3D model with the 1D and 2D

results discussed in this work. Fig. 10 shows the 3D radiation flux originating from the irregular surface, which is similar to its 2D counterpart. It suggests that the non-uniform and non-isotropic radiation flux is emitted from this surface. Large flux sites (hot spots) come from the dents of the shell, which reflect the impact of radiative cooling on the dynamics of colliding shells. Our results also suggest the region near the core is very turbulent. The turbulence may not affect the observational signatures of colliding shells, but it may affect the consequent core evolution. Finally, we compare the results from 2D and 3D rad-hydro models and find the 3D shell is thicker and smoother than the shell of the 2D model, as shown in Fig. 11.

5.2. 3D Light Curves

We show the 3D LCs from different viewing angles in Fig. 12. The peak luminosity of 3D LCs is about $1.8 - 2.3 \times 10^{43}$ erg sec $^{-1}$, and the second peak in the LC also smooths out. The peak of the light curve lasts about 100 days, then it enters a plateau region of $L \sim 2 - 3 \times 10^{42}$ erg sec $^{-1}$. When the photo-sphere is close to the colliding shell, radiation flux becomes more sensitive to the viewing angles.

6. DISCUSSION

1D evolution shows a big density spike formation, which turns into a deformed shell in 2D and an irregular surface in 3D. Regardless of the dimensionality of rad-hydro simulations, a thin dense shell eventually forms due to the radiative cooling. But multidimensional simulations suggest this shell should have non-spherical symmetry. To understand the intrinsic properties of shells, we plot the 1D angle-averaged density profiles from multi-D rad-hydro models and compare them with 1D results in Fig. 13. The 1D density spike forms regardless of the opacities chosen. Δ_S in the density spike easily exceeds 1000 within a few days after P3 launch. The spike truncates into multiple bumps of $\Delta_S \sim 100$ in 2D and 3D. These bumps also imply inhomogeneous and anisotropic radia-

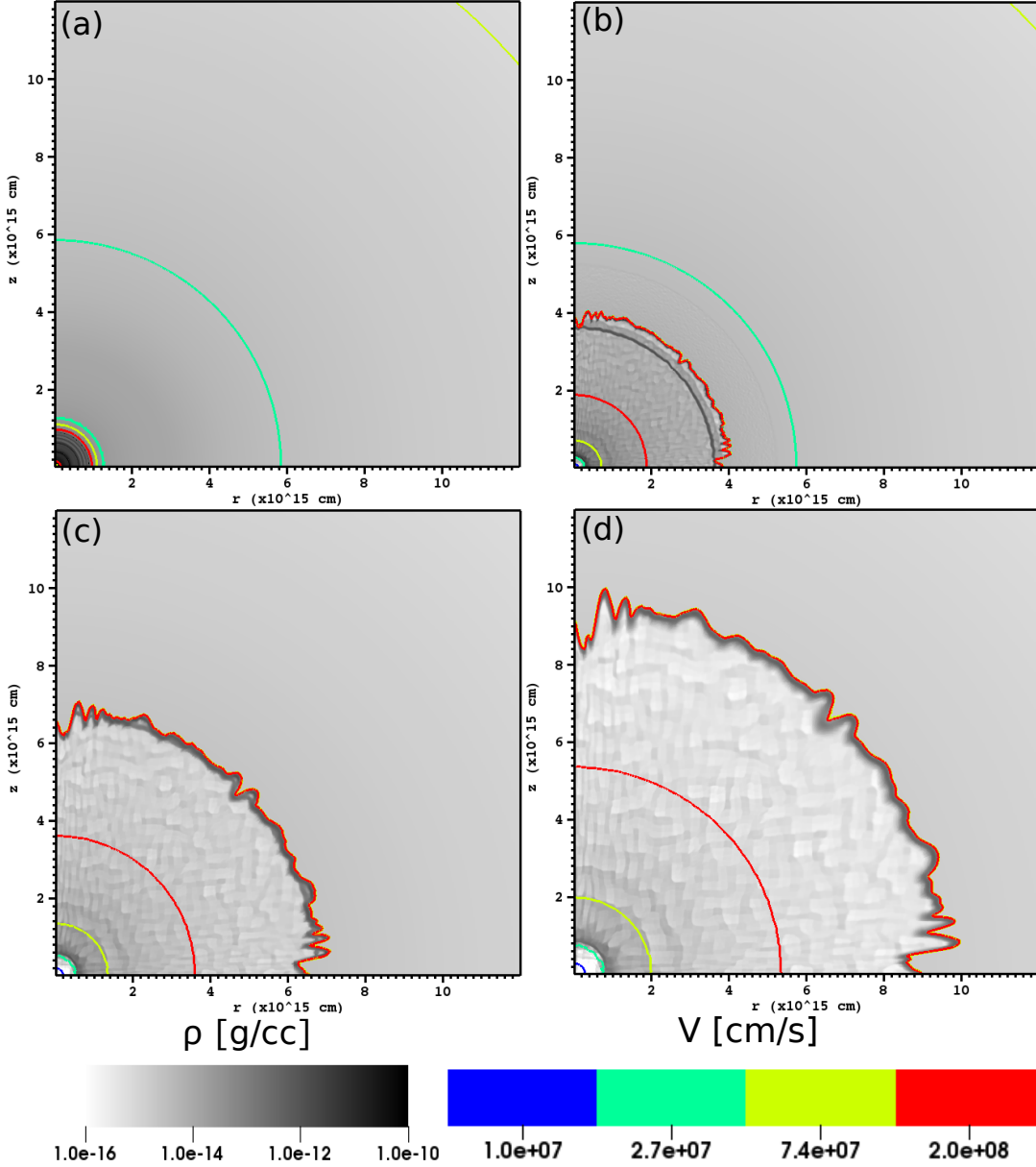


Figure 5. Evolution of gas density and velocity of the $\kappa = 0.2$ model in 2D. Panels (a), (b), (c), and (d) show the density and velocity at snapshots of 0, 100, 200, 300, and 400 days, respectively. A dense shell forms, and its shape is deviated from spherical symmetry with small-scale irregular structures. This shell travels at a velocity of $\sim 2 \times 10^8$ cm sec $^{-1}$.

tion emission of PPISNe in multi-D. Finer structures are found in the bumps of $\kappa = 0.2$ than $\kappa = 0.1$. A comparison of the same $\kappa = 0.2$ for 2D and 3D shows that the 3D seems to develop a thicker shell with fewer finer structures.

The total kinetic energy of P1 and P2 is $\sim 6 \times 10^{50}$ erg. Based on the LC results of 3D, the total radiation emitted until the shock passes $r \sim 10^{16}$

cm is about 1.64×10^{50} erg. Therefore, about 27% of the kinetic energy of P1+P2 is converted into radiation. Radiation released from the colliding shell can be estimated by using inelastic collisions (momentum conservation). For example, Pulses A and B have mass and velocity of M_a , V_a and M_b , V_b , respectively. If the thermal energy during the collision converts into radiation, the amount of radia-

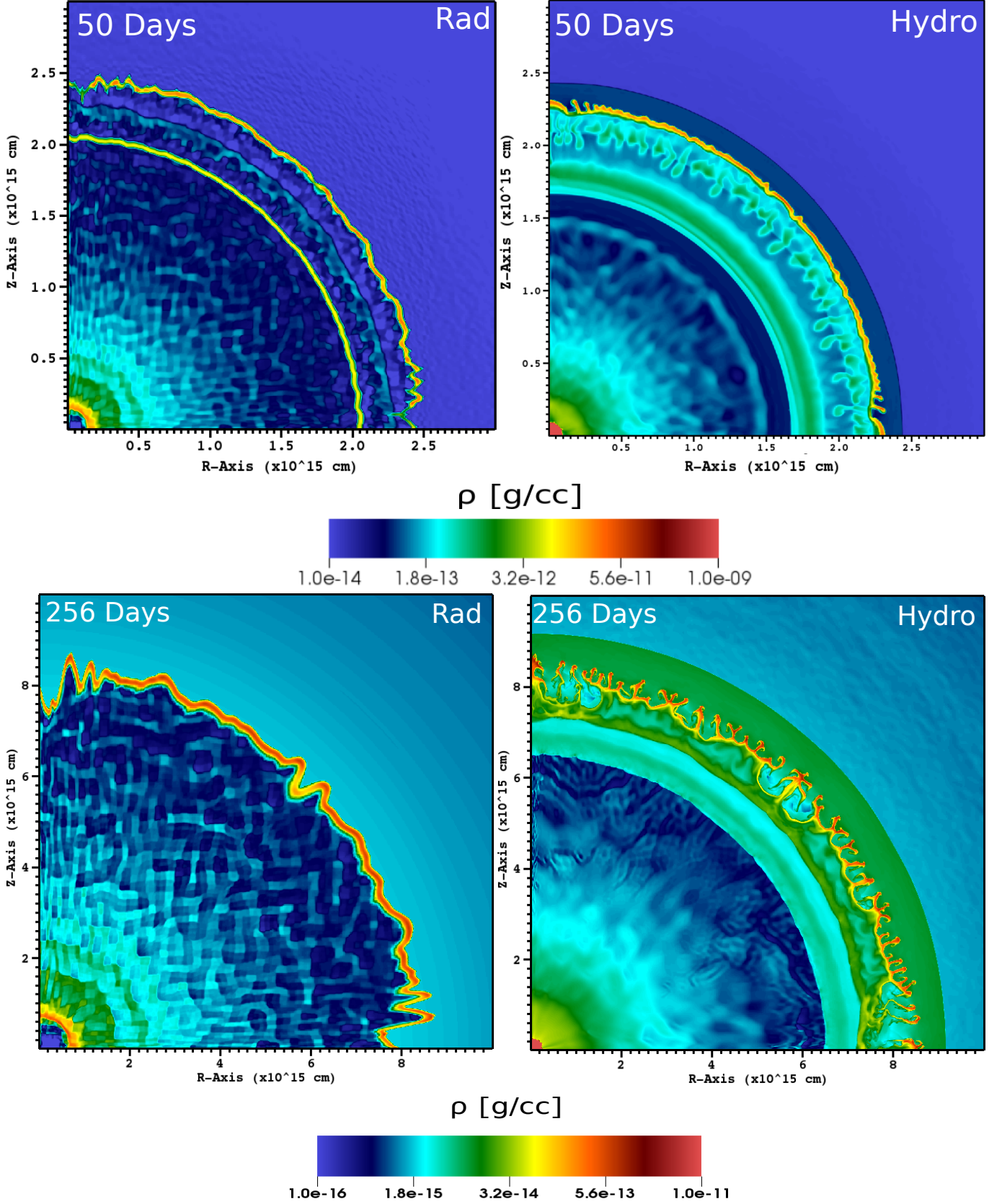


Figure 6. Density profiles of rad-hydro and pure-hydro at 50 and 256 days since the P3 eruption. In the rad-hydro model ($\kappa = 0.2$), the shock front does not produce a visible density discontinuity. Fluid instabilities are also smeared out in the rad-hydro model. At 256 days, the pure-hydro results show visible RT fingers and the shock front (the outer green arc); however, these features are invisible in the rad-hydro run.

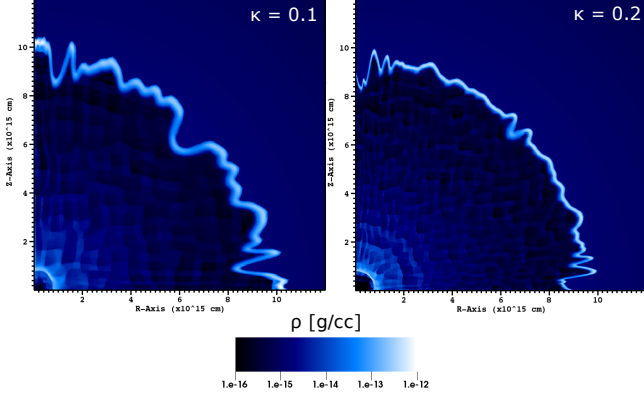


Figure 7. 2D density profiles of $\kappa = 0.1$ and $\kappa = 0.2$ at 300 days after the collisions. Both show the formation of the irregular dense shell. The width of the shell in $\kappa = 0.1$ is slightly thicker than that of $\kappa = 0.2$.

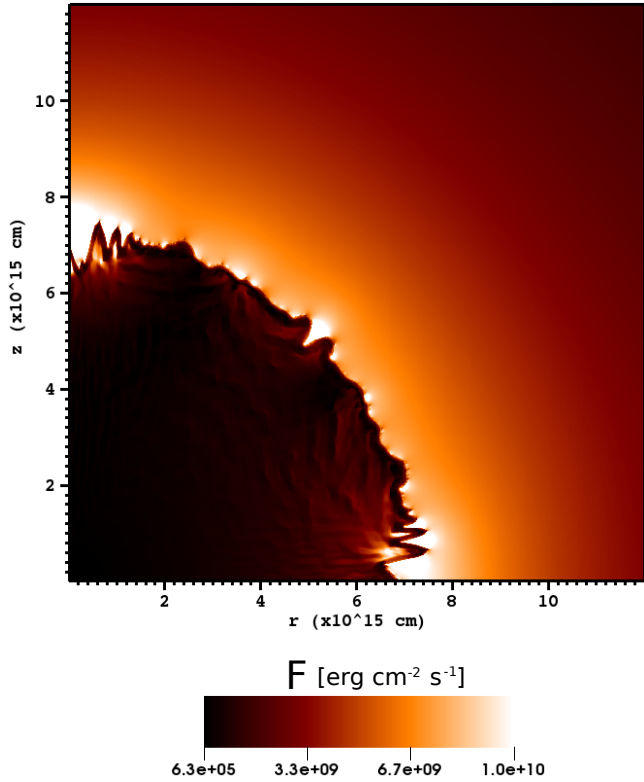


Figure 8. 2D radiation flux at 212 days. The hot spots of radiation flux appear right in front of the colliding regions. These spots are randomly distributed and suggest the non-homogeneous emission of the PPISNe.

tion can be expressed as

$$E_r \sim \frac{M_a M_b}{M_a + M_b} (V_a - V_b)^2. \quad (4)$$

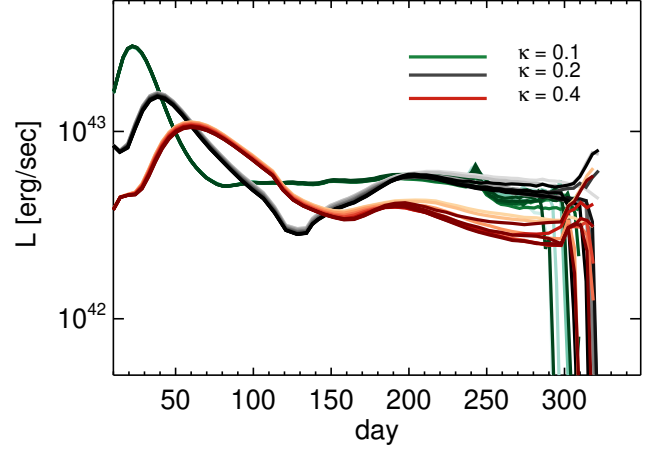


Figure 9. LCs of 2D models. The LCs are calculated from rad-hydro models of $\kappa = 0.1$, $\kappa = 0.2$, and $\kappa = 0.4$. In each model, there are ten LCs from different viewing angles from $\theta = 0 - 90$ degree with gradual colors. The peak luminosity is around $1 - 3 \times 10^{43} \text{ erg sec}^{-1}$ and lasts for 50–120 days. The sharp double peak features seen in 1D are smoothed out in 2D. The late-time luminosity becomes more sensitive to the viewing angle dependence. The luminosity drops quickly when the colliding shell passes $r \sim 10^{16} \text{ cm}$.

By estimating the mass of P2+P3 and P1 to be $\sim 5M_\odot$ and $\sim 50M_\odot$ with $V_a - V_b \sim 2 \times 10^8 \text{ cm sec}^{-1}$, we obtain the amount of radiation energy $\sim 1.86 \times 10^{50} \text{ erg}$, which is consistent with our results.

We also compared the mixing of different elements in the rad-hydro and pure-hydro simulations. The mixing in the rad-hydro shows distinctive features from those found in the previous multidimensional pure-hydro simulations. PPISNe only eject heavy elements having atomic numbers below ^{28}Si . The iron group elements frequently seen in other types of SNe, such as ^{56}Ni , have not been seen in PPISNe. In the pure-hydro simulation, we found the mixing is distributed in a region of $\sim 2 - 3 \times 10^{15} \text{ cm}$. However, in the multidimensional rad-hydro runs, the mixture of ^{12}C and ^{16}O occurs in a shell with a thickness $< 5 \times 10^{14} \text{ cm}$, and $^{12}\text{C}/^{16}\text{O}$ have dredged up to the shock front, as shown in Fig. 14. The unique spectra feature of PPISNe has rich ^{12}C and ^{16}O but a deficiency in

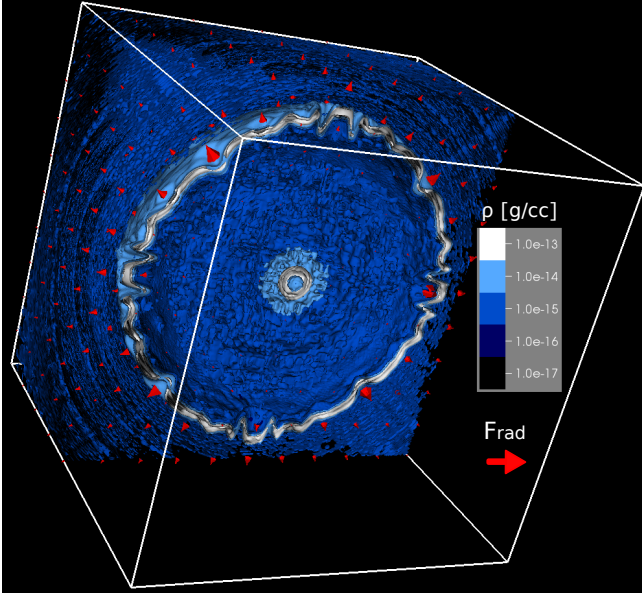


Figure 10. Density and radiation vector field from the 3D model at 260 days. A dense shell again forms in the 3D model. The radiation field is scaled with the size of the arrows based on its flux. The larger flux tends to originate from the dented regions of the shell.

^{28}Si and ^{56}Fe : Our results suggest this rapid mixing in the thin shell should also reflect on the spectra evolution at the peak of LC.

6.1. Toward Realistic Observational Signatures of PPISNe

The constant opacities in our simulation do not represent realistic situations. Opacities may vary dramatically in the photon trajectories due to sudden changes in ionization states of the gas. To provide sophisticated predictions of PPISNe, the first task is to improve the opacities of simulations by calculating the electron fraction with multi-species Saha equations or using comprehensive opacity tables. Once the realistic opacities become available, we can use multi-group rad-hydro simulations to obtain color LCs, which are very useful for probing the nature of PPISNe and guiding the observational strategies. Due to the lesser accuracy of the FLD method in the optically thin region, new radiation transfer schemes, such as Variable-Eddington-Tensor (Jiang et al. 2013; Davis et al. 2014, VET),

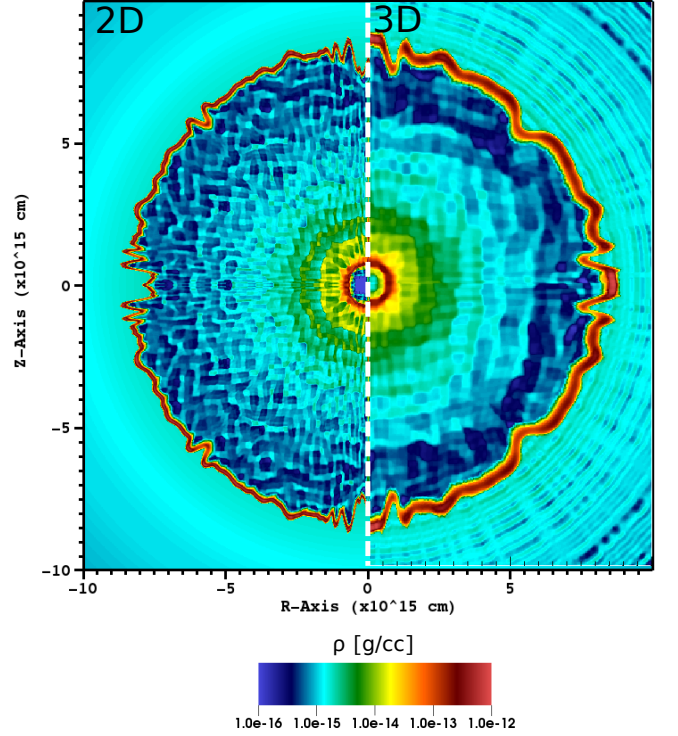


Figure 11. Comparison of density structures from 2D and 3D rad-hydro simulations at 250 days. The width of the 2D shell is thinner than the width of the 3D. There are also fewer fine structures in the 3D. The positions of the 2D and 3D shells are both at $r \approx 8 \times 10^{15}$ cm.

may address the rad fluid instabilities in the optically thin limit more accurately. In this paper, we present only one PPISN from a progenitor star of $110 M_{\odot}$. Next, we plan to carry out a grid of different progenitor stars based on Woosley (2017). Depending on the eruptions' energy and duration, PPISNe can provide observational signatures from radio to UV, and they will also be exciting targets for the current and coming observatories. However, the above improvements increase the technical difficulty of running rad-hydro simulations and boost the computation expense at the cost of tens of millions of CPU hours. The planned simulations will push the envelope of state-of-the-art computational astrophysics, and they will be feasible for years to come.

7. CONCLUSION

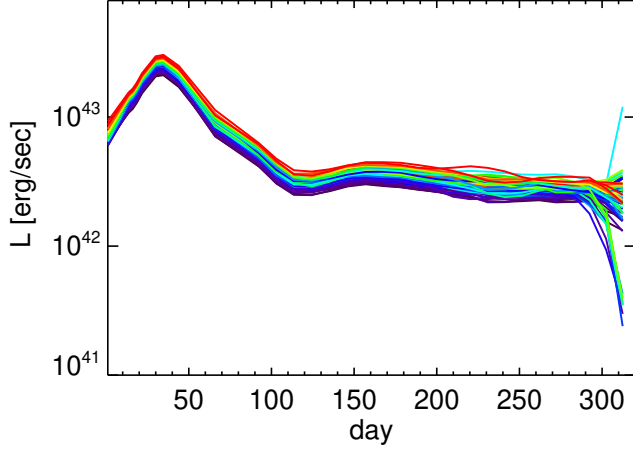


Figure 12. LCs from the 3D model. Different colors represent 25 LCs from different viewing polar angles $\theta = 0 - 180^\circ$ and azimuthal angles $\phi = 0 - 360^\circ$. The peak luminosity is $\sim 2 \times 10^{43} \text{ erg sec}^{-1}$ and lasts about 100 days. The late-time LCs start to vary greatly as the shell approaches our photosphere at $r \sim 10^{16} \text{ cm}$.

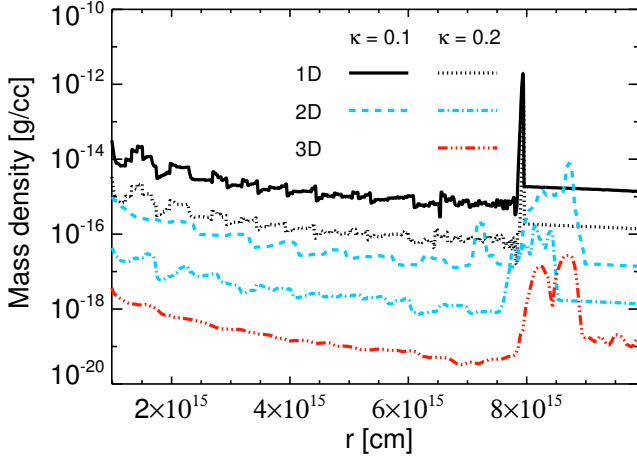


Figure 13. Angle-averaged density profiles of 1D, 2D, and 3D rad-hydro runs at 250 days (offseted for clarity). As the dimensionality increases, the density spike in 1D transforms to a broader and more noisy bump in 2D, and it is even more smooth in 3D. 2D results suggest the higher opacity would make the shell thinner with finer structures.

We have presented 1D, 2D, and 3D models of a PPISN from a $110M_\odot$ solar metallicity star by using rad-hydro simulations with CASTRO. Ear-

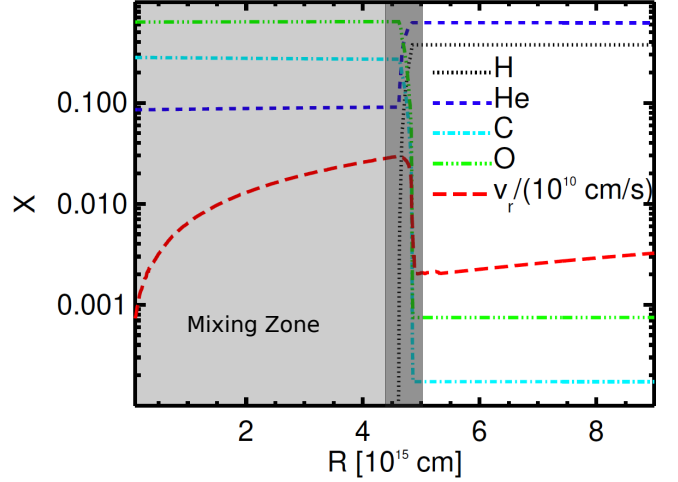


Figure 14. Angle-averaged elemental and velocity profiles of 2D rad-hydro runs at 135 days. The dark region indicates the position of the forward shock as well as the thin shell. Elements in the post-shocked region (gray shade) have been homogeneously mixed up.

lier 1D rad-hydro results (Woosley et al. 2007; Woosley 2017) have suggested a big density spike formation that implies the fluid instabilities, and follow-up 2D pure-hydro simulations by (Chen et al. 2014) showed the development of RT instabilities. Our 1D rad-hydro simulation resolves the structure of the spike found in previous studies, and the resulting LCs are more smooth. Both resolution and opacity can affect ejecta dynamics and emission. There is a second peak feature in the 1D LCs, and it comes from the subsequent collision of the two thin shells of P2 and P3. The 1D density spikes truncate into multiple bumps, and the second peak feature of LC is smoothed out in the 2D and 3D runs. The results of 2D rad-hydro are different from their pure-hydro counterparts. The forward-shock feature and the reverse-shock-driven mixing are less prominent than those in previous 2D pure-hydro models. The radiative cooling dissipates the forward shock's velocities of pulses and transforms them into thin shells. Therefore, it results in a weak reverse shock and a weak mixing. An irregular shell starts emitting with inhomogeneous and anisotropic flux to power LCs.

We conclude by stating the characteristics of a representative PPISN of a $110 M_{\odot}$ star. The peak of bolometric LCs is about $8-20 \times 10^{42}$ erg sec $^{-1}$ with a duration of 100–200 days with a second peak possibly appearing at 100–150 days after the first peak, but it may just appear to be a broad bump in the LCs. There is a long plateau phase of $2-3 \times 10^{42}$ erg sec $^{-1}$ lasting for 150–200 days, and it is possibly sensitive to its viewing-angle. About 27% of the kinetic energy of P1 and P2 are converted into radiation. The ejecta are dominated by ^4He , ^{12}C , and ^{16}O .

The luminous PPISNe provide a powerful probe to the early universe and also open new windows on massive star formation in both the local and primordial universe. With the advancement of models and new data taken from coming transit factories, such as the *Zwicky Transient Facility* (ZTF) and the *Large Synoptic Survey Telescope* (LSST), we shall soon gain a better understanding of PPISNe. Our multidimensional radiation transport simulations shed light on the important characteristics of PPISNe. In our future papers, we will build new models, including new radiation schemes, realistic opacities, a large grid of models to obtain sophisticated light curves, and spectra of PPISNe.

We thank the members of CCSE at LBNL for help with CASTRO. We also thank Stan Woosley and Alexander Heger for providing the KEPLER models. KC thanks Dan Kasen, Ann Almgren, Lars Bildsten, and Ken Nomoto for many useful discussions. This research is supported by an EA-COA Fellowship, and by the Ministry of Science and Technology, Taiwan, R.O.C. under Grant no. MOST 107-2112-M-001-044-MY3. KC thanks the hospitality of the Aspen Center for Physics, which is supported by NSF PHY-1066293, and the Kavli Institute for Theoretical Physics, which is supported by NSF PHY-1748958. Numerical simulations are supported by the National Energy Research Scientific Computing Center (NERSC), a U.S. Department of Energy Office of Science User Facility operated under Contract No. DE-AC02-05CH11231; the Center for Computational Astrophysics (CfCA) at National Astronomical Observatory of Japan (NAOJ); and the TIARA Cluster at the Academia Sinica Institute of Astronomy and Astrophysics (ASIAA).

REFERENCES

- Arcavi, I., Howell, D. A., Kasen, D., et al. 2017, *Nature*, 551, 210
- Almgren, A. S., et al. 2010, *ApJ*, 715, 1221
- Barkat, Z., Rakavy, G., & Sack, N. 1967, *Physical Review Letters*, 18, 379
- Blinnikov, S. I., Röpke, F. K., Sorokina, E. I., Gieseler, M., Reinecke, M., Travaglio, C., Hillebrandt, W., & Stritzinger, M. 2006, *A&A*, 453, 229
- Chatzopoulos, E., & Wheeler, J. C. 2012a, *ApJ*, 748, 42
- . 2012b, *ApJ*, 760, 154
- Chatzopoulos, E., Wheeler, J. C., & Couch, S. M. 2013, *ApJ*, 776, 129
- Chen, K., Heger, A., & Almgren, A. S. 2011, *Computer Physics Communications*, 182, 254
- Chen, K.-J., Heger, A., & Almgren, A. S. 2013, *Astronomy and Computing*, 3, 70
- Chen, K.-J., Woosley, S., Heger, A., Almgren, A., & Whalen, D. J. 2014, *ApJ*, 792, 28
- Chen, K.-J. 2015, *Modern Physics Letters A*, 30, 1530002
- Chevalier, R. A., & Imamura, J. N. 1982, *ApJ*, 261, 543
- Chevalier, R. A., & Irwin, C. M. 2011, *ApJL*, 729, L6
- . 2012, *ApJL*, 747, L17
- Colella, P., & Woodward, P. R. 1984, *Journal of Computational Physics*, 54, 174
- Commerçon, B., Teyssier, R., Audit, E., Hennebelle, P., & Chabrier, G. 2011, *A&A*, 529, A35+
- Cooke, J., et al. 2012, *Nature*, 491, 228
- Davis, S. W., Jiang, Y.-F., Stone, J. M., et al. 2014, *ApJ*, 796, 107.
- Dessart, L., Hillier, D. J., Waldman, R., Livne, E., & Blondin, S. 2012, *MNRAS*, 426, L76

- Dessart, L., Waldman, R., Livne, E., Hillier, D. J., & Blondin, S. 2013, *MNRAS*, 428, 3227
- Dessart, L., Audit, E., & Hillier, D. J. 2015, *MNRAS*, 449, 4304
- Dolence, J. C., Burrows, A., & Zhang, W. 2015, *ApJ*, 800, 10
- Fryxell, B. et al. 2000, *ApJS*, 131, 273
- Gal-Yam, A., et al. 2009, *Nature*, 462, 624
- González, M., Audit, E., & Huynh, P. 2007, *A&A*, 464, 429
- Hayes, J. C., Norman, M. L., Fiedler, R. A., Bordner, J. O., Li, P. S., Clark, S. E., ud-Doula, A., & Mac Low, M.-M. 2006, *ApJS*, 165, 188
- Heger, A., & Woosley, S. E. 2002, *ApJ*, 567, 532
- Heger, A., Woosley, S. E., Martínez-Pinedo, G., & Langanke, K. 2001, *ApJ*, 560, 307
- Inserra, C., Bulla, M., Sim, S. A., & Smartt, S. J. 2016, *ApJ*, 831, 79
- Ivezic, Z., et al. 2008, *arXiv:0805.2366*
- Jerkstrand, A., Smartt, S. J., & Heger, A. 2016, *MNRAS*, 455, 3207
- Jiang, Y.-F., Davis, S. W., & Stone, J. M. 2013, *ApJ*, 763, 102
- Kaiser, N., et al. 2002, in *Society of Photo-Optical Instrumentation Engineers (SPIE) Conference Series*, Vol. 4836, Society of Photo-Optical Instrumentation Engineers (SPIE) Conference Series, ed. J. A. Tyson & S. Wolff, 154–164
- Kasen, D., & Bildsten, L. 2010, *ApJ*, 717, 245
- Kasen, D., Woosley, S. E., & Heger, A. 2011, *ApJ*, 734, 102
- Krumholz, M. R., Klein, R. I., McKee, C. F., & Bolstad, J. 2007, *ApJ*, 667, 626
- Law, N. M., et al. 2009, *PASP*, 121, 1395
- Leung, S.-C., Nomoto, K., & Blinnikov, S. 2019, *arXiv:1901.11136*
- Moriya, T. J., Blinnikov, S. I., Tominaga, N., Yoshida, N., Tanaka, M., Maeda, K., & Nomoto, K. 2013, *MNRAS*, 428, 1020
- Lovegrove, E., Woosley, S. E., & Zhang, W. 2017, *ApJ*, 845, 103
- Moriya, T. J., & Langer, N. 2015, *A&A*, 573, A18
- Timmes, F. X., & Swesty, F. D. 2000, *ApJS*, 126, 501
- Volonteri, M. 2012, *Science*, 337, 544
- Weaver, T. A., Zimmerman, G. B., & Woosley, S. E. 1978, *ApJ*, 225, 1021
- Whalen, D. J., Fryer, C. L., Holz, D. E., Heger, A., Woosley, S. E., Stiavelli, M., Even, W., & Frey, L. H. 2013a, *ApJL*, 762, L6
- Whalen, D. J., Smidt, J., Even, W., Woosley, S. E., Heger, A., Stiavelli, M., & Fryer, C. L. 2014, *ApJ*, 781, 106
- Whalen, D. J., et al. 2013c, *ApJ*, 777, 110
- . 2013d, *ApJ*, 768, 195
- . 2013e, *ApJ*, 778, 17
- Smidt, J., Whalen, D. J., Chatzopoulos, E., et al. 2015, *ApJ*, 805, 44
- Woosley, S. E. 2010, *ApJL*, 719, L204
- Woosley, S. E., Blinnikov, S., & Heger, A. 2007, *Nature*, 450, 390
- Woosley, S. E. 2017, *ApJ*, 836, 244
- Woosley, S. E. 2018, *ApJ*, 863, 105
- Swesty, F. D., & Myra, E. S. 2009, *ApJS*, 181, 1
- Takahashi, K. 2018, *ApJ*, 863, 153
- van der Holst, B. et al. 2011, *ApJS*, 194, 23
- Zhang, W., Howell, L., Almgren, A., Burrows, A., & Bell, J. 2011, *ApJS*, 196, 20
- Zhang, W., Howell, L., Almgren, A., Burrows, A., Dolence, J., & Bell, J. 2013, *ApJS*, 204, 7